Advanced Laboratory Course
S264: Radio Astronomical Observing Course

Martin Ludwig, Amelia Carina de Lope Fend

31.03.2025

Contents

1 Introduction

Radio astronomy offers us a new perspective on the universe and allows us to study phenomena that optical astronomy cannot detect, such as sources that do not emit visible light or are shielded by dust clouds. A special focus of radio astronomy is the HI 21 cm line, which corresponds to the characteristic radio emission of neutral hydrogen. In this experiment, we conduct HI line measurements with the Stockert 25 m radio telescope. The aim is to become familiar with the construction and working principles of such a telescope, as well as with the observation procedures and data reduction techniques.

During the experiment, we first observe the calibration source S7 to determine the ratio between the measured antenna temperature and the brightness temperature of the observed object. With this calibration factor in hand, we continue by observing the galaxy NGC 5457 (also known as M101). From its measured HI line shape, we wish to determine its mass. Finally, we point the telescope at the pulsar PSR B0355+54 and record its periodic signal across multiple frequency bands. With these observations, we can determine the pulsar's dispersion measure and subsequently its distance.

This report is structured as follows. Chapter 2 provides a brief overview over the theoretical concepts that are needed for the experiment's analysis. Chapter 3 describes the general setup of a radio telescope as well as the characteristics of the Stockert telescope. Chapter 4 describes our measurements and their analysis, specifically the calibration, the galaxy's mass determination and the pulsar's dispersion measure determination. Finally, our results are summarized in Chapter 5.

2 Theoretical Background

Since the analysis of the experimental data requires several formulas, these formulas and the underlying theoretical concepts shall be briefly introduced in this chapter. Unless stated otherwise, all the presented information is taken from [1].

2.1 HI Observations

Hydrogen is by far the most prevalent element in space. While some of it is contained in stars, a major part exists as diffuse gas in the interstellar medium (ISM) or the intergalactic medium (IGM). There it can appear in molecular, atomic, or ionic form. Neutral atomic hydrogen (denoted by HI) emits characteristic radiation that allows us to detect it. This radiation is caused by a hyperfine transition in the ground state (1s): the spins of the proton and the electron can either couple to a total spin of $F = 0$ (antiparallel) or $F = 1$ (parallel), with the latter state having a slightly higher energy. Consequently, the excited state transitions into the ground state by a spin-flip via photon emission at $\lambda = 21.11\,\mathrm{cm}$ corresponding to $\nu = 1420.41\,\mathrm{MHz}$ [2].

While the $F = 1$ state is populated by collisions, the transition probability for de-excitation is extremely small. This leads to a very long lifetime of about 11×10^6 yr and, according to Heisenberg's uncertainty principle, to a very narrow linewidth. However, due to the velocity of the hydrogen atoms, the line shape is broadened thermally and turbulently, eventually leading to a Gaussian line profile that is much broader than the natural linewidth.

2.1.1 Column Density and HI Mass

When we observe the HI 21 cm line from a specific source, we are usually interested in the amount of hydrogen that produces this line. This quantity is called the column density and is defined as the number of HI atoms per unit area along the line of sight. To calculate it, we assume that all emitted HI photons actually reach us, i.e. they are not scattered or absorbed along the way (in this case we call the gas *optically thin*). Then the column density N_{HI} can be found by integrating over the line profile:

$$\frac{N_{\mathrm{HI}}}{\mathrm{cm}^{-2}} = 1.8224 \cdot 10^{18} \int \frac{T_B}{\mathrm{K}} \frac{\mathrm{d}v}{\mathrm{km\,s}^{-1}} \, , \tag{2.1}$$

where T_B denotes the brightness temperature and v is the relative velocity between the telescope and the observed HI source. The latter can be directly related to the observed

frequency ν via the Doppler equation

$$v = \left(1 - \frac{\nu}{\nu_0}\right) \cdot c, \tag{2.2}$$

with c being the speed of light and $\nu_0 = 1420.41\,\text{MHz}$ the frequency of the unshifted HI line.

As explained later in Section 3.4.3, the measured brightness temperature T_B can be converted to the specific flux S_ν. If the distance D to the HI source is known, we can calculate its HI mass in a similar way as in Eq. 2.1, eventually leaving us with:

$$\frac{M_{\text{HI}}}{M_\odot} \simeq 2.36 \cdot \times 10^{-7} \left(\frac{D}{\text{Mpc}}\right)^2 \int \frac{S_\nu}{\text{Jy}} \frac{\mathrm{d}v}{\text{km s}^{-1}} . \tag{2.3}$$

The HI mass of a galaxy is at most $10\,\%$ of its baryonic mass. To obtain the total mass of a galaxy, dark matter needs to be taken into account as well. The ratio of the luminous mass to the dark matter contained in a galaxy depends on its morphology, as shown in Figure 2.1.
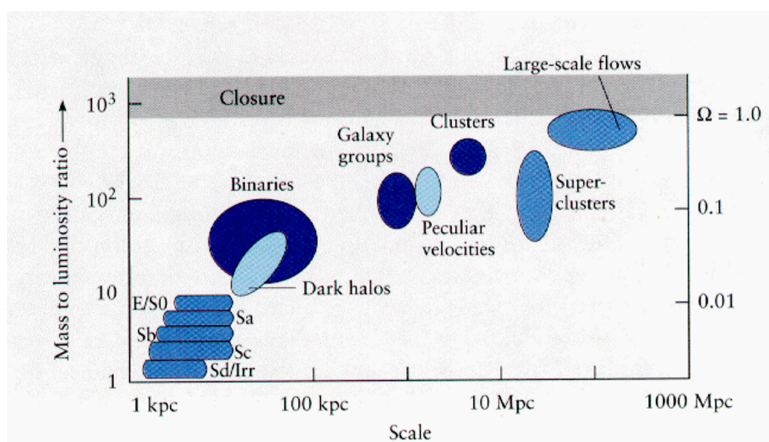

Figure 2.1: Mass to luminosity ratio for different linear scales, taken from [1].

2.2 Pulsars and Their Dispersion Measure

At the end of their life, massive stars of about 10 to 20 solar masses undergo a core-collapse supernova and produce a neutron star. These are extremely dense objects with a mass of 1 to $3M_\odot$ compressed into a sphere with a radius of about 10 to 15 km. The conservation of the initial star's angular momentum causes neutron stars to rotate with very high frequencies. Furthermore, they have very high magnetic fields.

A pulsar is a neutron star whose rotation axis is not aligned with the axis of the magnetic field. Due to the strong electromagnetic fields, charged particles are accelerated and form two beams along the magnetic axis. If one of the beams points toward Earth,

we see the pulsar blinking like a lighthouse. Their highly periodic radiation pulses have periods ranging from milliseconds to seconds.

If one observes a pulsar's signal over a small frequency range, one notices that its arrival time depends on the frequency ν. The reason for this is that on its way to the telescope, the pulsar radiation interacts with the ISM. The ISM is partly ionized, for example due to UV radiation, meaning that there is a small number of free electrons n_e per unit volume. The interaction with the free electrons leads to a frequency-dependent slowing down of the pulsar radiation. One can show that the time difference Δt between a wave packet traveling through the ISM versus one traveling through perfect vacuum is given by

$$\Delta t(\nu) = \frac{e^2}{2\pi m_e c} \frac{1}{\nu^2} \int_0^d n_e \, \mathrm{d}l \,, \tag{2.4}$$

where e is the elementary charge, m_e the electron mass, c the speed of light, and d the distance to the pulsar. The integrated density of free electrons is called the dispersion measure (DM) of the pulsar: $\mathrm{DM} = \int_0^d n_e \, \mathrm{d}l$. Inserting common astronomical units into Eq. 2.4, one finds

$$\frac{\Delta t(\nu)}{\mathrm{s}} = 4.15 \cdot 10^3 \left(\frac{\mathrm{MHz}}{\nu} \right)^2 \frac{\mathrm{DM}}{\mathrm{pc \, cm^{-3}}} \,. \tag{2.5}$$

3 Radio Telescopes

The information presented in this section is based on [1] and partly on the tour that the operator gave us on site.

3.1 General Construction and Working Principle

A radio telescope is an instrument that collects and enhances incoming radio waves. For this purpose, incoming radiation is focused by a parabolic dish and then processed by a receiving system (a so-called radiometer). In principle, there are two options for the placement of the receiver. Either the receiver is mounted at the prime focus of the main dish, or an elliptical or hyperbolic secondary dish is used to reflect the incoming radiation a second time so that it reaches the receiver located behind the center of the primary dish. The Stockert 25 m telescope uses the prime-focus design. This approach has the advantage of being simpler and therefore cheaper as well as easier to manufacture, align, and maintain.
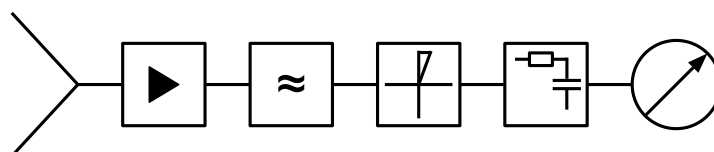

Figure 3.1: Schematic drawing of the principal construction of a radiometer. Adapted from [1].

Figure 3.1 shows a schematic drawing of a radiometer. It contains the following units (we follow the discussion of [1] here): The first part is a tapering waveguide known as the feed horn. It collects the radio waves and is optimized for certain frequencies. Inside the waveguide, standing waves establish and are converted into electric currents via an antenna. To be sensitive to all possible polarizations, one vertical and one horizontal antenna is used.

Since the received radiation is very faint, the electrical signals from the antenna must be amplified, typically by a factor of 10^3 to 10^6. Due to these high gains, it is essential to suppress noise at this stage. To achieve this, the amplifier must either be cooled to very low temperatures or be constructed using highly pure semiconductors, which is the approach used at the Stockert telescope.

Subsequently, the signal passes through a bandpass filter to isolate the frequency range of interest before being squared using a diode and integrated with an RC circuit.

Squaring the signal prior to integration is necessary because otherwise the positive and negative voltage components would cancel each other out. Finally, the integrated signal is read out and further processed by the backend electronics.

3.2 Surface Accuracy

Practically, every dish has exhibits deviations σ from the ideal parabolic shape. These imperfections may lead to destructive interference if they are on the same order of magnitude as the wavelength λ being observed. Consequently, one tries to keep the deviations much smaller than the wavelength. A quantity that measures the quality of the dish is the so-called surface accuracy:

$$\eta = \exp\left(-\left(\frac{4\pi\sigma}{\lambda}\right)^2\right)$$

In the ideal case where $\sigma \ll \lambda$, the surface accuracy attains values close to 1, while for larger deviations η becomes smaller.

In the case of HI 21 cm line observations, rather high deviations are still acceptable and it is even possible to build the dish from mesh. This approach is also used at the Stockert telescope. According to the telescope's web page [3], the dish's average deviation is $\sigma = 1.7$ mm and the maximal deviation is $\sigma = 4$ mm. With $\lambda = 21.11$ cm, this leads to average and maximal surface accuracies of $\eta = 0.99$ and $\eta = 0.94$, respectively.

3.3 Antenna Diagram and Half Power Beam Width

Every telescope exhibits a characteristic sensitivity distribution to incoming radiation. This means that not only is radiation received from the direction the telescope is pointing at, but also, in smaller amounts, from next to or even from behind the telescope. The projection of the telescope's three-dimensional sensitivity onto the azimuth plane is called the antenna diagram. In this diagram, the sensitivity is plotted in decibels versus the angle, with 0 dB corresponding to the maximum sensitivity. This maximum value is reached in the so-called main lobe, which typically collects around 70 % of the total incoming radiation. The so-called side and back lobes, on the other hand, collect radiation from the sides or from behind the telescope, thereby contaminating the signal of interest. These lobes should be kept as small as possible.

As a measure of the extent of the main lobe, the half power beam width (HPBW) is typically specified. This is defined as the angle at which the sensitivity has dropped to half (i.e. approximately -3 dB). The HPBW determines the degree to which two separate objects can still be resolved and, in practice, can be calculated using the formula

$$\text{HPBW} = 58.9 \cdot \frac{\lambda}{D},$$

where λ is the observed wavelength and D denotes the diameter of the dish. For the Stockert 25 m telescope and the observation of the HI 21 cm line, this results in a half power beam width of HPBW $\approx 0.5°$.

3.4 Temperatures

The signal measured by a telescope can be expressed as a temperature. However, not only does the source of interest contribute to this temperature, but also a significant amount of background radiation including the cosmic microwave background (CMB), synchrotron radiation from the Milky Way, emission from our atmosphere, radiation from beyond the edges of the dish (so-called spill-over), and noise from the receiver. The sum of all these contributions yields the system temperature T_{sys}. Consequently, in order to extract the brightness temperature of the source, the other contributions must be filtered out by fitting and subtracting the baseline.

3.4.1 Radiometer Equation

To estimate the uncertainty ΔT on the measured brightness temperature of an observed source, one can make use of the radiometer equation

$$\Delta T = \frac{T_{\mathrm{sys}}}{\sqrt{\Delta\nu \cdot \Delta t}}\,. \tag{3.1}$$

Here, $\Delta\nu$ denotes the bandwidth and Δt the duration of the observation.

3.4.2 Antenna Temperature and Brightness Temperature

Another important consideration regarding temperature measurements is that, even after baseline subtraction, the so-called antenna temperature T_{A} measured by the telescope does not directly correspond to the actual brightness temperature T_{B} of the source. The reason for this lies in the difference between the angular extent of the source Ω_{Source} and that of the main beam $\Omega_{\mathrm{MainBeam}}$. Usually, the source does not fill the full beam but only a part of it, while the rest of the beam collects background radiation unrelated to the source. Since the amount of this unrelated background radiation varies with time, the ratio between the measured antenna temperature and the source's brightness temperature must be determined prior to each observation:

$$\frac{T_B}{T_A} = \frac{\Omega_{\mathrm{Source}}}{\Omega_{\mathrm{MainBeam}}} = \alpha\,. \tag{3.2}$$

For this purpose, a calibration measurement is performed (see Section 4.1). This means that a calibration source with a well-known brightness temperature is observed to determine α. Then, the temperatures from subsequent measurements are multiplied by this factor to obtain the actual brightness temperatures.

7

3.4.3 Conversion from Kelvin to Jansky

In some cases it is desirable to convert the brightness temperature measured by the telescope into the specific flux S_{source} of the source. The quantity that enables this conversion is the telescope-dependent aperture efficiency A_{eff}:

$$A_{\text{eff}} = \frac{P_{\text{received}}}{S_{\text{source}}}\,.$$

Here, P_{received} is the received power from the source, which is, according to the Rayleigh-Jeans approximation, proportional to the measured brightness temperature: $P_{\text{received}} = 2k_{\text{B}}T$, with k_{B} being Boltzmann's constant. Inserting the specific values for the Stockert telescope yields

$$\frac{T/\text{K}}{S_{\text{source}}/\text{Jy}} = 0.09\,. \tag{3.3}$$

4 Measurements and Analysis

Now that the theoretical foundation is laid and we are familiar with the telescope and its characteristics, we describe our measurements and their analysis. This includes the calibration (Section 4.1), the mass determination of the galaxy NGC 5457 (Section 4.2) and the DM determination of PSR B0355+54 (Section 4.3).

4.1 Calibration

4.1.1 Preparation

First we need to find a calibration source that is visible during our observation slot. The Script [1] recommends the three options for the calibration source: the standard regions S7, S8 and B8, which are located within the plane of the Milky Way galaxy . The coordinates of the standard regions are provided in the paper by Kalberla et al. (1982) [4], Table 2. Using these, we can select a source that is located above the horizon during our observation slot. We check this by using airmass.org [5]. The result for our date and time of observation (12:00 - 15:00 on the 31st of March 2025) is shown in Figure 4.1. We conclude that S7 is best suited, as the other two sources are located closer to the horizon, which increases the amount of interference.
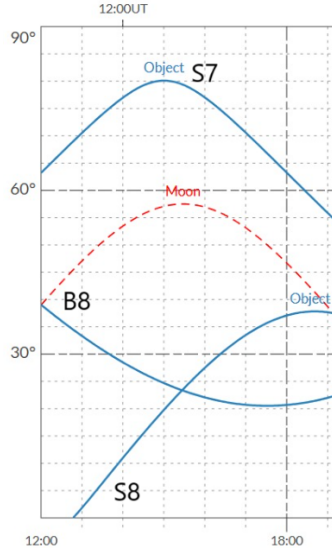
Figure 4.1: Position of the possible calibration sources during observation time, determined using airmass.org [5]. The Y-axis shows the elevation, the upper x-axis the local time.

4.1.2 Measurement

We observe the emission at a central frequency of $\nu = 1.420\,405\,752\,0\,\text{GHz}$ of standard region S7 for an observation time of $\tau =$ 19.796 78 s. This is a sufficient integration time, as S7 is a bright source. We will verify this later on in the analysis. The frequency resolution per channel is $\Delta\nu = 6103.515\,625\,\text{Hz}$. The resulting raw spectrum is shown in Figure 4.2. The data provides both the channel number and the frequency corresponding to the Antenna Temperature.
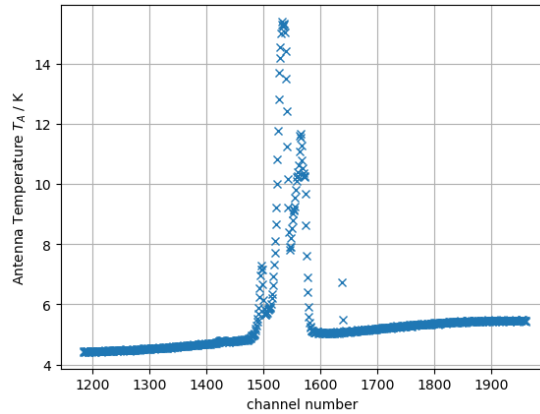

Figure 4.2: Raw spectrum of the standard region S7.

10

4.1.3 Data Analysis

Baseline reduction

Due to background noise the Antenna Temperature is higher than zero even in regions that don't contain the source. In order to remove this baseline we apply a polynomial fit to it. To do so, we remove the part of the data we identify as the signal from S7 as well as a bump, which corresponds to a High Velocity Cloud (HVC) and Radio Interference (RI). The latter one appears at the exact frequency corresponding to the 21 cm line. This corresponds to the following intervals:

$$\textbf{S7:} \quad \nu \in [1420.155\,\text{MHz}, 1421.064\,\text{MHz}] \quad n \in [1464, 1614]$$
$$\textbf{RI:} \quad \nu \in [1419.996\,\text{MHz}, 1420.002\,\text{MHz}] \quad n \in [1639, 1640]$$
$$\textbf{HVC:} \quad \nu \in [1421.211\,\text{MHz}, 1421.431\,\text{MHz}] \quad n \in [1404, 1439]$$

Here the frequencies are listed, as these were used to asses the physical meaning as well as the channels, as this was used to perform the fit. The intervals are also depicted in Figure 4.11a. We apply a polynomial fit to the remaining baseline

$$f(x) = ax^3 + bx^2 + cx + d,$$

which yields

$$a = -\,3.060(78) \times 10^{-9}\,\text{K}$$
$$b = 1.427(37) \times 10^{-5}\,\text{K}$$
$$c = -\,2.030(58) \times 10^{-2}\,\text{K}$$
$$d = 1.36(30)\,\text{K}$$

and it is depicted in Figure 4.3. As the data was treated as data without uncertainty, computing the χ^2/ndf value does not make sense here.

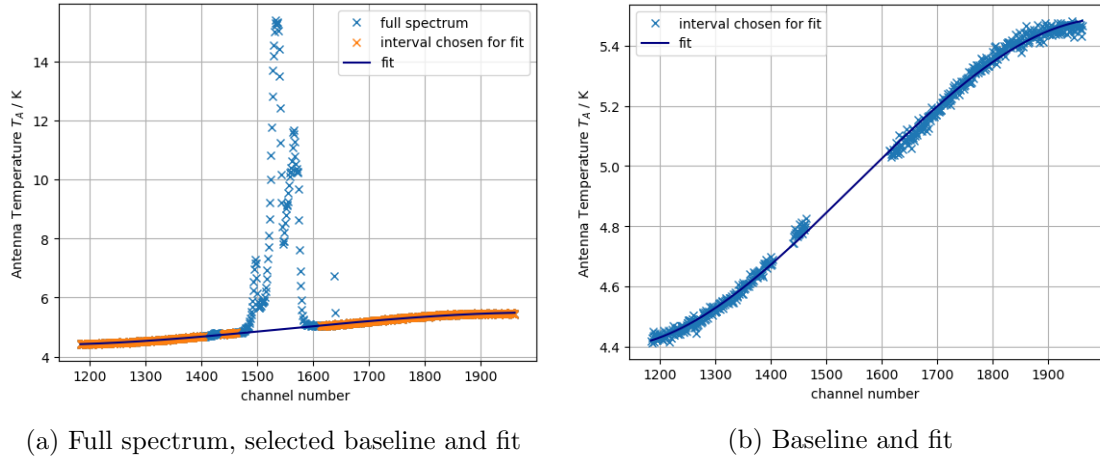(a) Full spectrum, selected baseline and fit   (b) Baseline and fit

Figure 4.3: Raw spectrum of the standard region S7, selected baseline for fit and fit.

After subtracting the baseline, we convert the frequencies corresponding to the channels into recessional velocities v via the Doppler equation 2.2. The results are shown in Figure 4.4.
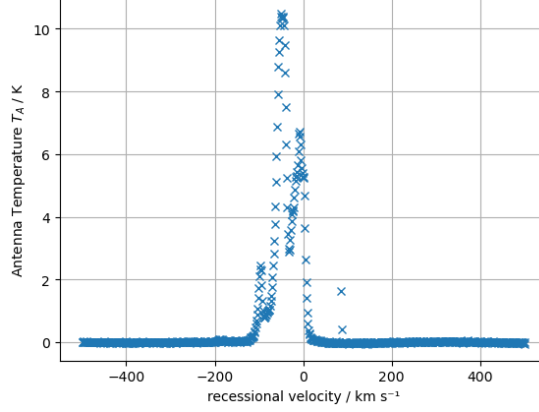

Figure 4.4: Full spectrum of S7 after removing the baseline and converting to recessional velocities

Uncertainty of T_A and accuracy

Now reduced baseline lies at $T = 0\,\text{K}$, as expected. To estimate the uncertainty of the Antenna Temperature, we calculate the Root-Mean-Square (RMS) value of the reduced baseline

$$\Delta T_A = \sqrt{\frac{\sum_{\nu \in \text{baseline}} T_A^2}{N}} = 0.018\,\text{K}$$

Originally we aimed for minimum 5% accuracy, which is given for all Antenna Temperatures $T_A > 0.36\,\text{K}$. So in regards to the source, this condition was fulfilled and the observation time of $\tau = 19.8\,\text{s}$ was indeed sufficient.

Calibration factor α

After removing the baseline, the maximum value of the spectrum is $T_{A,max} = 10.488\text{K}$. Using the value of HPBW $= 0.5°$ obtained in Section 3.3, we can read off the corresponding value for the Brightness Temperature Figure 4 in the paper by Kalberla et al. (1982 [4]) as $T_{B,max} = 95.8(2)\text{K}$. Inserting these into

$$\alpha = \frac{T_{B,\text{max}}}{T_{A,\text{max}}}$$

where the uncertainty on α was computed using gaussian error propagation

$$\alpha = 9.13(13).$$

Unless stated otherwise gaussian error propagation will be the default to compute any uncertainty. Using this, we can compute the Brightness Temperature spectrum, shown in Figure 4.5.
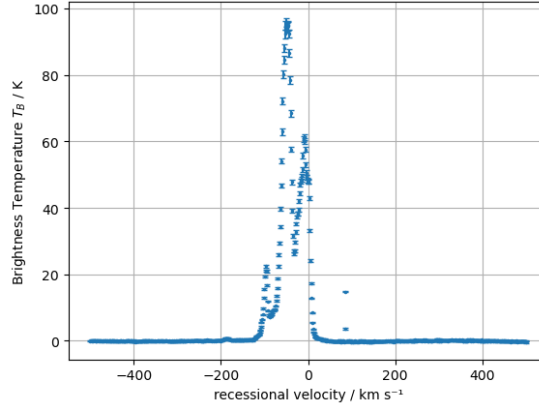

Figure 4.5: Full Spectrum of S7 after baseline reduction and conversion to Brightness Temperature.

System Temperature

Using the uncertainty of the Antenna Temperature and the Radiometer Equation 3.1 we can compute the System Temperature T_{sys}. This yields

$$T_{\text{sys}} = \alpha \cdot \Delta T_A \cdot \sqrt{\tau \cdot \Delta\nu}$$

Inserting the bandwidth $\Delta\nu = 6103.515\,625\,\text{Hz}$ and integration time of $\tau = 19.796\,78\,\text{s}$ and the value for $\alpha = 9.13(13)$ results in

$$T_{\text{sys}} = 57.15(79)\text{K}.$$

This is significantly higher than the typical temperature for cooled systems of $18\,\text{K}$ mentioned in the script [1], however, the Stockert telescope is not cooled so a higher temperature is still plausible.

4.2 HI Mass of a Galaxy

4.2.1 Preparation

Before conducting the measurement, we need to find a suited galaxy. For this, we consider the following criteria:

- **Visibility of the source:** Analogously to the calibration source, we need to ensure that the galaxy is located above the horizon during our observation slot.

- **Peak line intensity** M**:** A galaxy with a high magnitude at the HI line is preferable, as this lowers the SNR and thus requires a smaller observation time.

- **Radial velocity** v **of the galaxy:** For very large radial velocities, we can not use the Hubble-Lemaitre law to deduce the galaxy's distance. Thus we pre-select galaxies with $v \in [-500\,\mathrm{m\,s^{-1}}, 500\,\mathrm{m\,s^{-1}}]$. However if the galaxy has a low recessional velocity, the spectrum might overlap with contributions from the milky way. To avoid this, when selecting galaxies don't consider those with recessional velocities close to zero.

- **Line width** Δv**:** The larger the area under the line profile, the larger the mass. We are interested in massive galaxies, however a broader line profile corresponds to a lower SNR.

- **Line shape:** Additionally the shape of the line profile depends on the inclination of the galaxy. With increasing inclination, the line shape will include two Doppler peaks at its edges (double horn profile), from which we can deduce the rotational velocities. This enables us to calculate the mass via a second approach. However this possible if the galaxy has no inclination.

We can search for matching galaxies using the Goddard space flight center's web interface [6]. We find that the Galaxy NGC 5457, also referred to as Messier 101 (M101), fits the criteria. According to [6], the values of the parameters of interest are

$$M = 10.39\,\mathrm{mag}$$
$$v = 240\,\mathrm{km\,s^{-1}}$$
$$\Delta v = 147\,\mathrm{km\,s^{-1}}$$

We check its visibility using airmass.org [5]. Figure 4.6 shows that its located above the horizon during observation time, although its rather low. We find the line profile of M101 in the HI Nearby Galaxy Survey [7], see Figure 4.7, which shows a double horn profile.
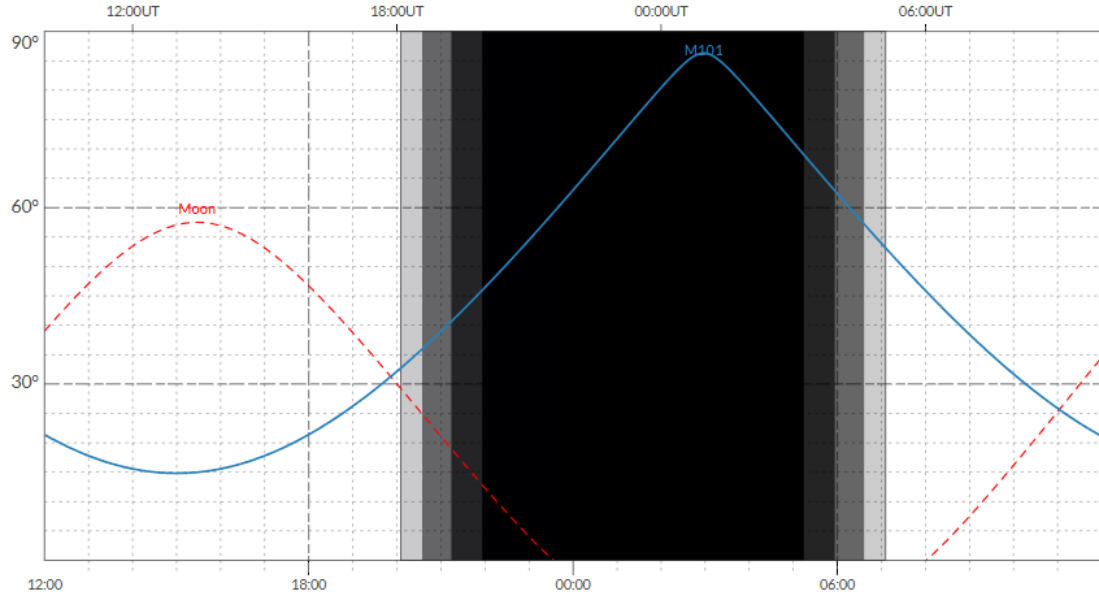
Figure 4.6: Position of the M101 during observation time, determined using airmass.org [5].
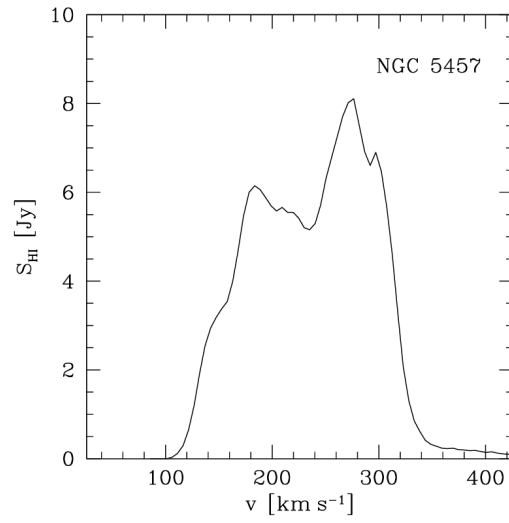

Figure 4.7: Global HI profile of M101, also referred to as NGC 5457, taken from the H I Nearby Galaxy Survey [7]. The Y-axis shows the elevation, the upper x-axis the local time.

4.2.2 Measurement

We measure the HI line of the spiral galaxy M101, located at DEC $54°21'2''$ and RA $14^{\mathrm{h}}\,03^{\mathrm{min}}$ 12.8^{sec}, again with a frequency resolution of $\Delta\nu = 6103.515\,625\,\mathrm{Hz}$. The integration time was $\tau = 593.900\,284\,\mathrm{s}$. The resulting raw spectrum is depicted in Figure 4.8.

Other sources will also contribute to the spectrum. We can account for these by conducting an off target measurement, which we archive by changing the telescopes position by $2°$ in elevation and azimuth. The resulting data is also shown in Figure 4.8.
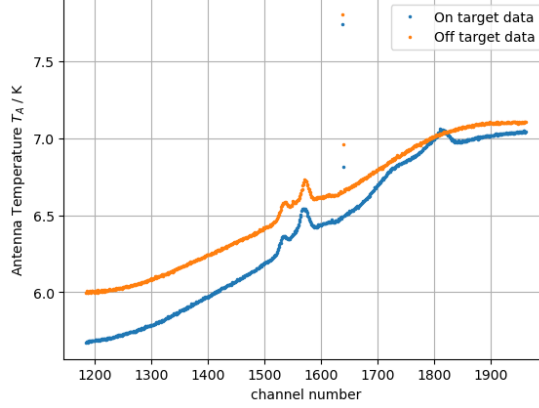

Figure 4.8: Raw spectrum of the galaxy M101 together with off target measurement.

4.2.3 Data Analysis

Uncertainty of T_A and accuracy

We aim for an accuracy of minimum $10\,\%$. We can check whether this integration time was sufficient to achieve that by using the Radiometer Equation 3.1 and our results for the System Temperature $T_{\mathrm{sys}} = 57.15(79)\mathrm{K}$. We could not do this before or while conducting the experiment, as the System Temperature was not known at that point, but we can asses whether the integration time was sufficient in retrospect. We obtain

$$\Delta T_{A,\mathrm{M101}} = 0.0300(41)\mathrm{K},$$

so any data with an Antenna Temperature above $0.300(41)$ K will be minimum 10 % accuracy. The resulting raw spectrum Figure 4.8 shows that all data points have a sufficiently high Antenna Temperature for minimum 10 % accuracy. As Antenna Temperatures exceed $3\,\mathrm{K}$, the data has minimum 1% accuracy and thus integration time was sufficient.

Subtracting the off target measurement

We convert to velocities, again using the Doppler Equation 2.2, which is depicted in Figure 4.9.
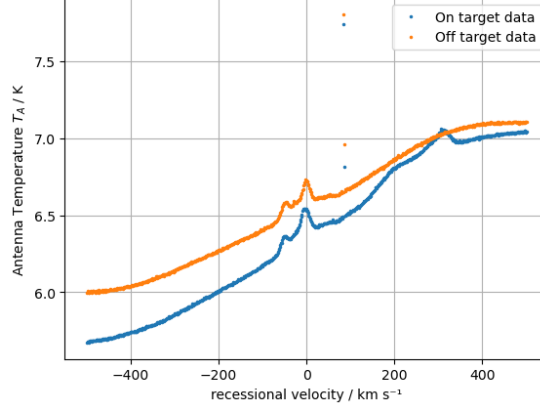
Figure 4.9: Full spectrum of the M101 on and off target measurement after converting to recessional velocities.

To separate the Signal from the background, we subtract the off target data with Antenna Temperature $T_{A,\text{off}}$ from the on target data with Antenna Temperature $T_{A,\text{M101}}$. This is possible because the integration time was identical.

$$T_A^* = T_{A,\text{M101}} - T_{A,\text{off}}$$

We convert to Brightness Temperatures using the conversion factor $\alpha = 9.13(13)$ derived in Subsection 4.1.3

$$T_B^* = \alpha \cdot T_A^*$$
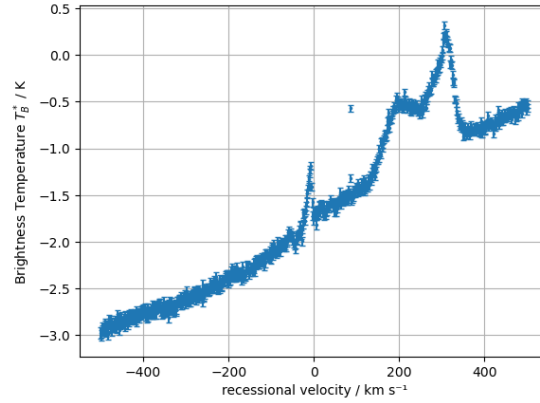
The resulting spectrum is shown in Figure 4.10.

Figure 4.10: Full spectrum of the M101 after subtracting the off target measurement from the on target measurement and converting to Brightness Temperature.

The plots shows negative temperatures in Kelvin, which as physical temperatures, are not plausible. However we are looking at a difference of two spectra here.The low recessional velocity peak around $0\,\text{km}\,\text{s}^{-1}$ corresponds to sources in the milky way. The signal

17

in the interval of roughly $v \in [180\,\mathrm{km\,s^{-1}}, 350\,\mathrm{km\,s^{-1}}]$ matches the signal we expect from M101, as it seems to display the expected double horn profile and on first glance agrees with the values for line width and velocity outlined in Subsection 4.2.1. This is also supported by the on and off target spectrum differing significantly in this region. The very narrow peak at $85.1\,\mathrm{km\,s^{-1}}$ and $86.4\,\mathrm{km\,s^{-1}}$ corresponds to the Radio Interference signal, which also appeared in the S7 spectrum. It differed slightly for the on and off target measurement and it thus still present after subtracting the off target data.

Baseline reduction

The next step is analogous to the analysis of the data of the standard region S7. We first select the intervals where we would expect the Brightness Temperature to be zero, as there should be no signal from a source or interference. The intervals are as follows:

$$
\begin{aligned}
\textbf{M101:} \quad & v \in [131.5\,\mathrm{km\,s^{-1}}, 369.8\,\mathrm{km\,s^{-1}}] \\
\textbf{RI:} \quad & v \in [85.1\,\mathrm{km\,s^{-1}}, 86.4\,\mathrm{km\,s^{-1}}] \\
\textbf{Milky way:} \quad & v \in [-61.7\,\mathrm{km\,s^{-1}}, 22.0\,\mathrm{km\,s^{-1}}]
\end{aligned}
$$

Again we fit a polynomial

$$f(x) = ax^3 + bx^2 + cx + d,$$

and obtain the fit parameters

$$
\begin{aligned}
a = & -2.230\,497\,17(19) \times 10^{-9}\,\mathrm{K\,km^{-3}\,s^3} \\
b = & \,1.452\,785\,0(14) \times 10^{-7}\,\mathrm{K\,km^{-2}\,s^2} \\
c = & \,2.937\,687\,84(29) \times 10^{-3}\,\mathrm{K\,km^{-1}\,s} \\
d = & -1.794\,786(21)\,\mathrm{K}
\end{aligned}
$$

We also obtain $\chi^2/ndf = 0.947$, which is close to 1 and indicates that the data is described well by the fitted function. The spectrum, the interval identified as baseline and the fit, as well as the spectrum after subtracting the baseline are depicted in Figure 4.11.

(a) Full spectrum, selected baseline and fit

(b) Baseline and fit

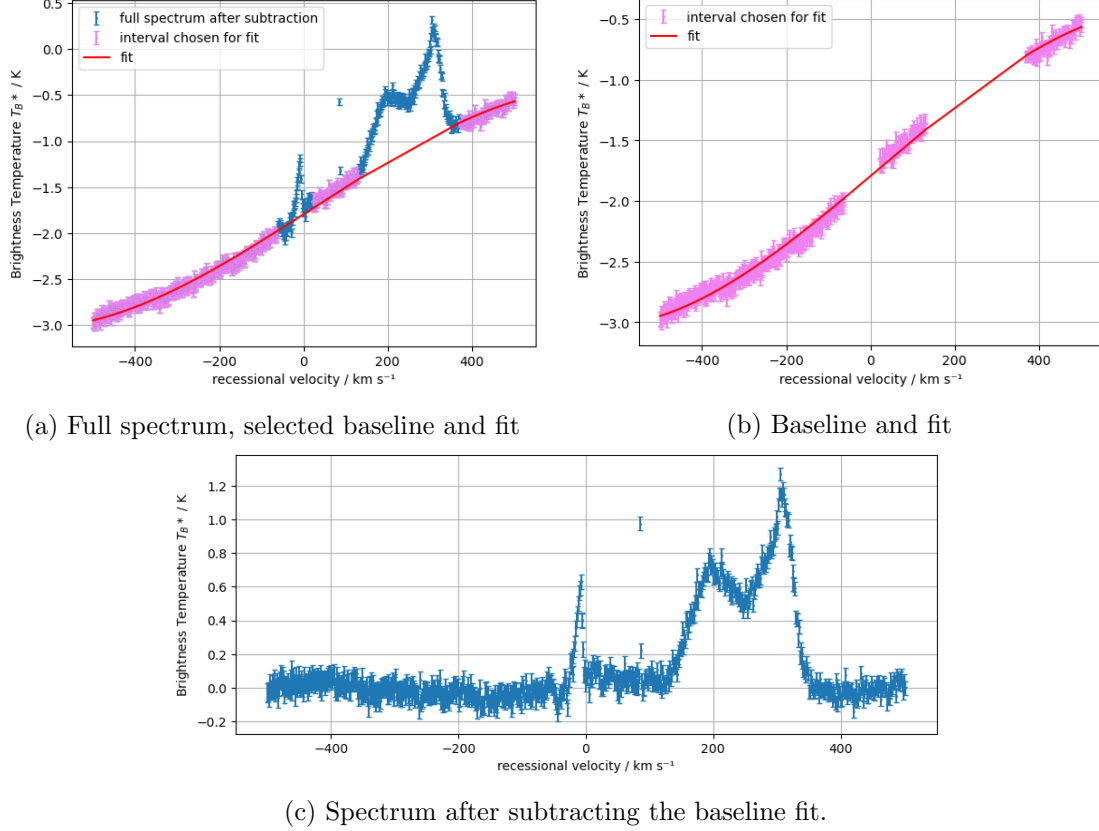(c) Spectrum after subtracting the baseline fit.

Figure 4.11: Spectrum of M101 after subtracting the off target measurement from the on target measurement and converting to Brightness Temperature and baseline fit.

After subtracting the fit for the baseline, we see that the new baseline is, as expected, distributed around $0\,\mathrm{K}$. This is important, as the line profile is going to be integrated over later on and a baseline deviating from $0\,\mathrm{K}$ would lead under or overestimating this integral.

When compared to the baseline corrected calibration spectrum, the uncertainties are quite large. This stems from the uncertainty of the conversion factor α and could have been reduced by increasing the time of observation of the calibration measurement.

Distance of M101

Using the Hubble–Lemaître law $H_0 D = v$, we can use the galaxy's recessional velocity v to estimate its distance. Here D is the distance and H_0 the Hubble constant. We assume that the broadening of the line is due to additional Doppler shift stemming from the galaxy's rotation and should thus be symmetrically distributed at equal distance from the outermost peaks. Therefore we find the recessional velocity in the middle of the outermost peaks. To estimate the position of the outermost peaks, we take the maximum

19

value of the curve in that region that corresponds to these peaks. This corresponds $v \in [150\,\mathrm{km\,s^{-1}}, 250\,\mathrm{km\,s^{-1}}]$ for the left peak and $v \in [250\,\mathrm{km\,s^{-1}}, 350\,\mathrm{km\,s^{-1}}]$ for the right peak.

We read off the maxima, which are also highlighted in Figure 4.12 along side the resulting recessional velocity of the galaxy v_{center}. We use the read-off error as uncertainty and obtain

$$v_{\mathrm{max,\ left}} = 194(10)\,\mathrm{km\,s^{-1}} \tag{4.1}$$

$$v_{\mathrm{max,\ right}} = 305(5)\,\mathrm{km\,s^{-1}} \tag{4.2}$$

$$v_{\mathrm{center}} = 250(11)\,\mathrm{km\,s^{-1}} \tag{4.3}$$

This seems to be a reasonable estimate, as the expected value $v_{\mathrm{catalogue}} = 240\,\mathrm{km\,s^{-1}}$ from the Goddard space flight center's galaxy catalogue [6] listed in Subsection 4.2.1 lies within the 1-σ interval. Inserting the experimentally determined value into the Hubble–Lemaître law using $H_0 = 75\,\mathrm{km\,s^{-1}Mpc^{-1}}$ given in the script [1] yields a distance D

$$D_{\mathrm{Hubble}} = 3.33(15)\,\mathrm{Mpc}.$$

This is approximately less than half of the value listed in the Goddard space flight center's galaxy catalogue $D_{\mathrm{Goddard}} = 7.38\,\mathrm{Mpc}$. This is because, according to [8], this value was determined using a different method: the measurement of Cepheid variables. For the remaining analysis, we will use $D_{\mathrm{Goddard}} = 7.38\,\mathrm{Mpc}$ as value for the distance.

HI mass of M101

To evaluate the HI mass of M101, we need to convert the Brightness Temperature T_B^* to specific flux S_ν. We do this using Equation 3.3 and the results for the relevant region are shown in Figure 4.12.
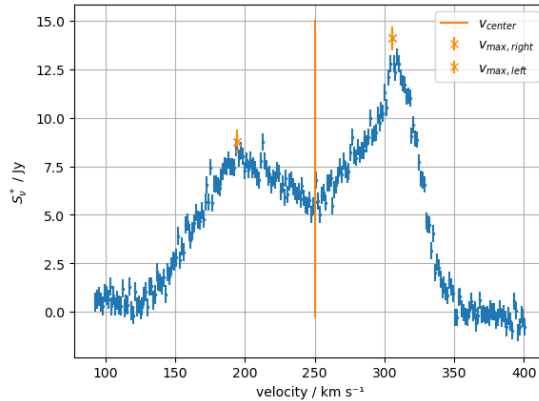

Figure 4.12: Line profile of M101 after converting to specific flux including peak and center velocities.

Finally we can estimate M101's HI mass using Equation 2.3

$$M_{HI} \simeq 2.36 \cdot \times 10^{-7} \left(\frac{D}{\mathrm{Mpc}} \right)^2 \int \left(\frac{S_\nu}{\mathrm{Jy}} \right) \cdot \left(\frac{dv}{\mathrm{km\,s^{-1}}} \right) \cdot M_\odot.$$

For this we need to compute the integral $I = \int \left(\frac{S_\nu}{\mathrm{Jy}} \right) \cdot \left(\frac{dv}{\mathrm{km\,s^{-1}}} \right)$. This is done using the Simpson's method. We chose the integration interval counting the galaxy's line profile by eye as $\nu \in [118.6\,\mathrm{km\,s^{-1}}, 376.3\,\mathrm{km\,s^{-1}}]$. To estimate the error we integrate over the uncertainty in the interval.

$$I = 1400(110)\,\mathrm{Jy\,km\,s^{-1}}$$

Finally, using the value from the the catalogue D_{Goddard}, the HI mass of M101 is

$$M_{\mathrm{HI}} = 17.3(14) \times 10^9 \cdot M_\odot$$

Baryonic mass of M101

According to the manual [1] the HI mass of a galaxy typically makes up at most 10 % of its total mass. Thus we arrive at a total baryonic mass $M_{tot,HI}$ of

$$M_{\mathrm{bar}} \leq 173(14) \times 10^9 \cdot M_\odot.$$

Total mass of M101

To derive the total mass from the baryonic mass, we can read off the ratio of luminous to dark matter from Figure 2.1. This requires the morphological type of M101, which according to [9] is SAB(rs)cd, which, in terms of the types listed in the plot, would correspond to an intermediate of c and d. We read off a factor f of $f = 10^k, k = 2(1)$ for the ratio of luminous matter to total matter and thus taking the upper bound for the uncertainty $f = 1.58(41)$. This yields a total mass of

$$M_{\mathrm{tot}} \leq 273(74) \times 10^9 \cdot M_\odot \tag{4.4}$$

In Table 2 in [10], the total mass of M101 is listed as $M_{\mathrm{lit}} = 230 \times 10^9 \cdot M_\odot$. This is consistent with our results, which lies below the upper limit on M_{tot}, within one standard deviation of the upper limit.

Alternative approach: total mass of M101 from rotational velocity

We can compute a very rough estimate of the total mass of M101 from its rotational velocity. For this, we assume that the gravitational force and the centripetal force are at equilibrium. Assuming the galaxy's mass M_{tot} is uniformly distributed in a sphere of radius $R = \frac{D}{2}$

$$M_{\mathrm{tot,rot}} = \frac{v_{\mathrm{rot,max}}^2 \cdot R}{G}, \tag{4.5}$$

with $G = 6.67430 \times 10^{-11} \mathrm{m^3\,kg^{-1}\,s^{-2}}$ [11] being the gravitational constant and $v_{\mathrm{rot,max}}$ being the rotational velocity of a probe mass at a distance R from the center of mass. This assumption deviates from the actual mass distribution significantly, as the mass distribution is not homogeneous and the mass is distributed in a flat disk. Therefore we expect the result to be less accurate and differ from the total mass derived via the HI mass. This section is only meant to provide a rough sketch of this method, as a more detailed calculation would require the galaxy's rotational curve (rotational velocity as a function of the distance from the center) and the focus of this report lies on the method using the HI mass. Thus a more detailed calculation would be out of scope.

The rotational velocity $v_{\mathrm{rot,max}}$ can be estimated from the galaxy's double horn profile and its inclination. The inclination of a galaxy is angle between the line-of-sight of the observer and the normal vector of the galaxy disk [12], $i = 22°$ [6]. If we assume that the outermost peaks of the line profile correspond to an emission from neutral Hydrogen at a distance of R from the galaxy's center of mass, we can find the value of the projection of their velocity onto the line-of-sight $v_{\mathrm{max,doppler}}$. This value corresponds to the difference

$$v_{\mathrm{max,doppler}} = |v_{\mathrm{max,\ left/right}} - v_{\mathrm{center}}| = 55(11)\,\mathrm{km\,s^{-1}}$$

for the values for $v_{\mathrm{max,\ left/right}}, v_{\mathrm{center}}$ listed in Equation 4.1 and were determined in Subsection 4.2.3. The resulting uncertainty of is quite large, as reading off the values is not a very precise method. We still need to correct for the inclination

$$v_{\mathrm{rot,max}} = \frac{v_{\mathrm{max,doppler}}}{\sin(i)} = 147(29)\,\mathrm{km\,s^{-1}}$$

The diameter d of the M101 is $d = 17 \times 10^4\,\mathrm{ly}$ [8], which translates to a radius of

$$R \geq 85 \times 10^3\,\mathrm{ly} = 80 \times 10^{19}\,\mathrm{m}. \tag{4.6}$$

Inserting these values into Equation 4.5 and using $M_\odot = 1.988 \times 10^{30}\,\mathrm{kg}$ [13] as well as

$$\Delta M_{\mathrm{rot,tot}} = \frac{2\Delta v_{\mathrm{rot,max}} \cdot v_{\mathrm{rot,max}} \cdot R}{G}$$

yields a total mass of $M_{\mathrm{rot,tot}}$

$$M_{\mathrm{rot,tot}} = 131(52) \times 10^9 \cdot M_\odot$$

This result lies within the same order of magnitude as the result derived from the HI mass, $M_{\mathrm{tot}} \leq 273(74) \times 10^9 \cdot M_\odot$, although they do not agree with each other within each others fist σ interval. But as outlined above, this was expected, because the second approach is simplified and relies on false assumptions (i.e. the mass being distributed uniformly with a sphere). The literature value $M_{\mathrm{bar,\ lit}} = 230 \times 10^9 \cdot M_\odot$ [10] is contained in the 2σ interval, however, keeping in mind that the uncertainty is very large, this does not hold a lot of significance. The HI method is requires less simplification, has a smaller relative uncertainty and more consistent with the literature method and thus clearly preferable.

4.3 Dispersion Measure of a Pulsar

4.3.1 Preparation

Prior to the observation, we have to decide which pulsar to observe. For this, we consider its visibility, its specific flux at the observed frequency of 1.4 GHz, and its dispersion measure (DM). We need to balance a high DM, which allows for a clearer separation of the signal's arrival time across different frequency bands, against signal strength, as a higher DM typically corresponds to a larger distance and therefore a fainter signal. Taking this into account, we can search the ATNF Pulsar Catalogue [14] for an appropriate candidate. We decided to choose PSR B0355+54 for the observation, as it has a relatively high DM of $57.1\,\mathrm{pc\,cm^{-3}}$ and, with a sufficiently long observation time, should still be detectable despite its relatively low flux density of 23 mJy at 1.4 GHz [14].

4.3.2 Measurement

For the observation of the pulsar, the operating mode of the backend electronics must first be changed. While for previous measurements of the HI spectra the signal was integrated over a certain period, in the pulsar mode the signal is stored every $218\,\mathrm{\mu s}$. This results in relatively large data streams (on the order of megabytes per second).

Since the pulsar radiation is relatively faint, measurements must be taken over a long period (in our case approximately 25 min) and the individual profiles must be folded so that the signal-to-noise ratio is high enough to make a pulse recognizable. For the folding process, the pulsar's period must be known. According to [14], for the observed PSR B0355+54 the period is $T = 156.4\,\mathrm{ms}$.

Finally, the signal is split into eight frequency bands. The observation is carried out with a bandwidth of 98.4 MHz and a maximum frequency of 1430.4 MHz. The subdivision results in a width of $98.4\,\mathrm{MHz}/8 = 12.3\,\mathrm{MHz}$ per band and a central frequency ν_k for the k-th band given by

$$\nu_k = 1430.4\,\mathrm{MHz} - \frac{2k-1}{2} \cdot 12.3\,\mathrm{MHz}\,. \tag{4.7}$$

The result of this data pre-processing is the folded pulsar signal over one period, divided into eight frequency bands. The time within the period is divided into 256 bins, and for each bin the intensity of the signal is stored. The bin width is given by

$$t_{\mathrm{bin}} = \frac{156.4\,\mathrm{ms}}{256} = 0.61\,\mathrm{ms}\,.$$

4.3.3 Data Analysis

The plotted pulsar signal for the eight frequency bands is shown in Figure 4.13. Overall, the pulses are relatively weak compared to the noise, especially in the last few bands. Nevertheless, it is apparent that the signal's arrival time shifts between the bands. To

quantify this more precisely, we fit the peak with a Gaussian function:

$$f(t) = A \cdot \exp\left(-\frac{(t-\mu)^2}{2\sigma^2}\right) + B \,. \tag{4.8}$$

Here, A is the signal amplitude, B is a constant offset, μ is the peak position, and σ is the width. The fit results are plotted as a black line in a 3σ interval around the peak in Figure 4.13. The determined fit parameters are listed in Table 4.1.
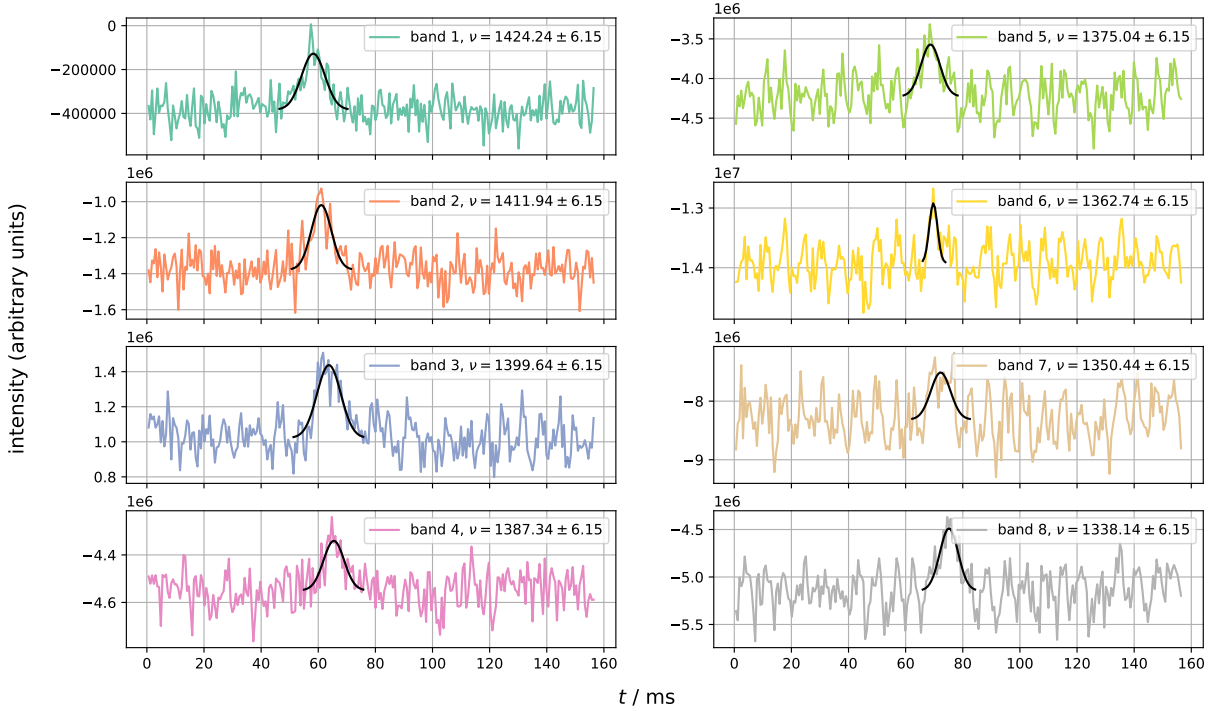

Figure 4.13: Pulsar signal over one period. The frequencies for each band were calculated according to Eq. 4.7. For each band, a Gaussian function was fitted to the signal (black line) to determine its arrival time.

From Eq. 2.5, we deduce that the DM can be calculated using the difference between two arrival times t and t' as well as their corresponding frequencies ν and ν':

$$\frac{\mathrm{DM}}{\mathrm{pc\,cm^{-3}}} = \frac{1}{4.15 \cdot 10^3} \frac{t - t'}{\mathrm{s}} \left(\left(\frac{\mathrm{MHz}}{\nu}\right)^2 - \left(\frac{\mathrm{MHz}}{\nu'}\right)^2\right)^{-1} \tag{4.9}$$

In principle, any pair of arrival times and frequencies can be used in this formula. However, it is sensible to choose values with a large time difference $t - t'$, as subtracting

Table 4.1: Fit parameters for the function 4.8 fitted to pulsar signal.

Band	ν / MHz	A / $[I] \cdot 10^5$	B / $[I] \cdot 10^6$	μ / ms	σ / ms
1	1424.24(615)	2.56(22)	$-0.383(4)$	58.3(4)	4.1(4)
2	1411.94(615)	3.59(32)	$-1.378(6)$	61.1(4)	3.5(4)
3	1399.64(615)	4.16(35)	$1.022(7)$	63.7(4)	4.2(4)
4	1387.34(615)	2.09(27)	$-4.549(5)$	65.5(5)	3.6(5)
5	1375.04(615)	6.5(9)	$-4.225(15)$	68.7(5)	3.3(5)
6	1362.74(615)	10.0(19)	$-13.92(2)$	69.7(3)	1.4(3)
7	1350.44(615)	8.0(15)	$-8.314(25)$	72.3(7)	3.4(7)
8	1338.14(615)	6.6(8)	$-5.144(13)$	75.2(4)	3.2(5)

two similar time values leads to larger relative errors. Therefore, we calculate the DM using the first and the last frequency bands, meaning that we insert $t = 75.2(4)$, $t' = 58.3(4)$, $\nu = 1424.24(615)$ and $\nu' = 1338.14(615)$ (see Table 4.1) into Eq. 4.9. This yields:

$$\text{DM} = 62(7)\,\text{pc}\,\text{cm}^{-3},$$

where the uncertainty was calculated using Gaussian error propagation. The obtained result agrees with the expected value of $57.1\,\text{pc}\,\text{cm}^{-3}$ [14] within the uncertainty range. Note that we used half the bandwidth as the uncertainty for the central frequencies, which contributes significantly to the uncertainty of the final result. Therefore, in order to conduct more precise measurements of the DM, the signal should be split into more and smaller frequency bands. This, in turn, requires a longer observation time, as otherwise the signal-to-noise ratio in each band would be too low.

As explained in Section 2.2, the dispersion measure is defined as the integrated number density of free electrons n_e. Consequently, if the pulsar's DM is known and an average value for n_e along the line of sight is assumed, its distance d can be calculated via

$$d = \frac{\text{DM}}{n_e}.$$

According to [1], a good estimate for the free electron number density is $n_e = 0.03\,\text{cm}^{-3}$. Using our result for the DM of PSR B0355+54, we find

$$d = 2.07(22)\,\text{kpc}.$$

A parallax measurement with the Very Long Baseline Array (VLBA) [15] revealed a distance of $1.04^{+0.21}_{-0.16}\,\text{kpc}$, which differs from our result by about 4σ. Since this parallax measurement does not rely on assumptions regarding n_e, we consider it to be more reliable than our estimate. Therefore, we conclude that the assumed value of $n_e = 0.03\,\text{cm}^{-3}$ is somewhat too low, at least along the line of sight to PSR B0355+54.

5 Conclusion

In this experiment, radio-astronomical observations were carried out using the Stockert 25 m telescope. After studying the basic design and operating principles of the telescope, the galaxy NGC 5457 (M101) and the pulsar PSR B0355+54 were observed during the observation session. The goal was to determine the HI mass and subsequently the total mass of the galaxy as well as the dispersion measure and the distance to the pulsar.

For the galaxy's mass determination, the telescope had to be calibrated first in order to determine the ratio between the brightness temperature and the antenna temperature. To do this, we observed the standard calibration source S7, whose brightness temperature is known. From the measurement, a calibration factor of $\alpha = 9.13(13)$ was obtained. To obtain the HI line profile of M101, an on and an off target measurement was conducted. Assuming an optically thin gas, the HI mass of the galaxy could be deduced from its line profile, resulting in $M_{\mathrm{HI}} = 17.3(14) \times 10^9 \cdot M_\odot$. Assuming the HI mass is at most 10% of its total mass and a ratio of total mass to luminous mass $f = 1.58(41)$ based on M101's morphology, the total was was determined as $M_{\mathrm{tot}} \leq 273(74) \times 10^9 \cdot M_\odot$. This is consistent with the total mass $M_{\mathrm{lit}} = 230 \times 10^9 \cdot M_\odot$ listed in [10].

The idea behind determining the pulsar's DM is to subdivide the periodic pulsar signal into several frequency bands. The dispersion manifests itself in the varying arrival time of the signal between the bands. By using pairs of arrival times and their corresponding frequencies, the DM of the observed PSR B0355+54 could be calculated as DM $= 62(7) \, \mathrm{pc \, cm^{-3}}$, which is in good agreement with the results of other studies. Assuming an average number density of free electrons $n_e = 0.03 \, \mathrm{cm^{-3}}$, the distance to the pulsar was calculated as $d = 2.07(22) \, \mathrm{kpc}$, which is roughly twice the value determined via parallax measurements. From this, we conclude that the assumed value for n_e along the pulsar's line of sight is somewhat too low.

List of Figures

List of Tables

Bibliography

[1] Jürgen Kerp. *Radio astronomical practical course at the Stockert 25-m telescope.* July 2022.

[2] Helmut Hellwig et al. 'Measurement of the Unperturbed Hydrogen Hyperfine Transition Frequency'. In: *IEEE Transactions on Instrumentation and Measurement* 19.4 (1970), pp. 200–209. DOI: 10.1109/TIM.1970.4313902.

[3] *Astropeiler Stockert.* 2025. URL: https://www.astropeiler.de/ (visited on 10/04/2025).

[4] Peter Kalberla, Ulrich Mebold and Klaus Reif. 'Brightness temperature calibration for 21-cm line observations'. In: *Astronomy and Astrophysics* 106 (1982), pp. 190–196. URL: https://api.semanticscholar.org/CorpusID:233116179.

[5] *Astronomical Object Visibility Plotter.* 2025. URL: https://airmass.org/ (visited on 03/04/2025).

[6] *GALAXY CATALOG.* 2025. URL: https://heasarc.gsfc.nasa.gov/db-perl/W3Browse/w3table.pl?tablehead=name%3Dneargalcat&Action=More+Options (visited on 03/04/2025).

[7] Fabian Walter et al. 'THINGS: The HI Nearby Galaxy Survey'. In: *The Astronomical Journal* 136.6 (Nov. 2008), pp. 2563–2647. ISSN: 1538-3881. DOI: 10.1088/0004-6256/136/6/2563. URL: http://dx.doi.org/10.1088/0004-6256/136/6/2563.

[8] *Messier 101.* 2025. URL: https://ned.ipac.caltech.edu/cgi-bin/objsearch?objname=NGC+5457&extend=no&hconst=73&omegam=0.27&omegav=0.73&corr_z=1&out_csys=Equatorial&out_equinox=J2000.0&obj_sort=RA+or+Longitude&of=pre_text&zv_breaker=30000.0&list_limit=5&img_stamp=YES (visited on 09/04/2025).

[9] *NED results for object NGC 5457.* 2025. URL: http://www.messier.seds.org/m/m101.html (visited on 09/04/2025).

[10] R. D. Davies, G. P. Davidson and S. C. Johnson. 'Neutral hydrogen in groups of galaxies – I. The inner M101 group'. In: *Monthly Notices of the Royal Astronomical Society* 191.2 (June 1980), pp. 253–268. ISSN: 0035-8711. DOI: 10.1093/mnras/191.2.253. URL: https://doi.org/10.1093/mnras/191.2.253.

[11] National Institute of Standards and Technology. *CODATA Value: Newtonian Constant of Gravitation.* URL: https://physics.nist.gov/cgi-bin/cuu/Value?bg (visited on 10/04/2025).

[12] *Inclination of Spiral Galaxies in a Snap.* 2025. URL: https://towardsdatascience.
      com / evaluating - the - spatial - inclination - of - disk - galaxies - with -
      tensorflow-bea0e53442d3/#:~:text=As%5C%20depicted%5C%20in%5C%20the%
      5C%20diagram%5C%20below%5C%2C%5C%20%5C%22%5C%20Inclination,of%
      5C%20the%5C%20projected%5C%20ellipse%5C%20that%5C%20defines%5C%
      20their%5C%20boundary. (visited on 10/04/2025).

[13] Andrej Prša et al. 'Nominal values for selected solar and planetary quantities: IAU
      2015 Resolution B3'. In: *The Astronomical Journal* 152.2 (Aug. 2016), p. 41. DOI:
      10.3847/0004-6256/152/2/41. URL: https://dx.doi.org/10.3847/0004-
      6256/152/2/41.

[14] *The ATNF Pulsar Catalogue.* URL: https://www.atnf.csiro.au/research/
      pulsar/psrcat/ (visited on 11/04/2025).

[15] Shami Chatterjee et al. 'Pulsar parallaxes at 5 GHz with the Very Long Baseline
      Array'. In: *Astrophys. J.* 604 (2004), pp. 339–345. DOI: 10.1086/381748. arXiv:
      astro-ph/0312044.